Efficient photocatalytic CO_2 reduction by visible-light responsive Fe-doped WO_3 nanostructures

Maryam Torabi Merajin[1], Mohammad Nasiri*[,1], Ebrahim Abedini[1] & Shahram Sharifnia[2]

[1]Department of Chemistry, Malek-ashtar University of Technology, Shahin-shahr P.O. Box 83145/115, Iran

[2]Catalyst Research Center, Chemical Engineering Depatment, Razi 67149-67246, Iran

E-mail: nasiri@mut.es.ac.ir

The nanoparticles of WO_3 doped with Fe ions have been employed for University, Kermanshah photocatalytic conversion of greenhouse gaseous of CO_2 and CH_4 under visible-light irradiation. The photocatalysts have been characterized by XRD, FESEM, EDX, Raman, UV-vis, and PL techniques. The XRD and Raman spectroscopies confirm the monoclinic structure of WO_3 nanoparticles and also the successful incorporation of Fe ions into WO_3 lattice. A red shift in Raman patterns of Fe-doped WO_3 samples indicate the partial substitution of W with Fe ions and the structural defects induced in WO_3 crystals upon doping treatment. The recorded PL signals reveal that the charge carrier recombination rate can be inhibited by doping WO_3 with Fe ions. The modified samples show high activity by photons with wavelength equal to/greater than ~500 nm, the visible-light in green region. The best photocatalytic reduction of CO_2 is provided to be 38.7% by WO_3 containing 4.18 at.% Fe under visible-light. Ethane, and formate and acetate derivatives are detected as the major products of CO_2 reduction.

Increasing atmospheric greenhouse gases (GHGs) caused by human activity has been considered as the major cause of global warming and global climate change, the observed rising the Earth's temperature over the current century[1]. CO_2 is the main GHG which seriously contributes to planet warming. The annual increasing atmospheric concentration of CO_2 is 0.4% and almost 80% of the increase is due to fossil fuels[2]. Hence, conversion of the extra CO_2 to C_1 chemicals is a main subject for the environmental researchers, not only for reducing the greenhouse effect but also for rectifying the natural balance of the global carbon cycle.

CO_2 is the most oxidation state of carbon, and accordingly, high energy is required to break the C-O bond. Over the past century, photocatalysis has offered an effective green route for the lab-scale transformation of CO_2 to useful organics like CO, CH_4, and CH_3OH[3,4]. By photocatalysis and without external energy input, CO_2 is reduced by capturing the photo-excited electrons of photocatalyst's CB (conduction band), and, at the same time, a reducing agent is oxidized by giving up electrons to the generated holes in photocatalyst's VB (valence band)[5]. CH_4 is a desirable reducing agent because it is also a GHG and supplies hydrogen required for useful hydrogenated chemicals.

A photocatalytic process in which the conversion of CO_2 and CH_4 takes place simultaneously is an ideal redox reaction.

A visible/UVA responsive photocatalyst, WO_3 absorbs visible photon up to 480 nm (~ 2.8 eV), so it is suitable for various photocatalytic purposes. It is easy to prepare, modify, and also is a harmless and stable metal oxide in acidic and oxidative conditions[6,7]. Narrowing the band gap of WO_3, to shift the photocatalytic activity to the shorter wavelengths, is possible by metal and non-metal doping. Doping of the photocatalyst often introduces a dopant-energy level in the middle of the original band gap of the host semiconductor[8]. Until now, some research groups have focused on the modification of WO_3 by metal elements such as Mg^9, Zn^{10}, Mo^{11}, V^{12}, Cu^{13}, Pt^{14}, and Ti^{15}. Fe is another metal element which is a good choice for insertion in WO_3 structure. Because of the same ionic radius of Fe^{3+} with that of W^{6+}, W ions can be expected to be substituted with Fe ions[16,17].

From the catalytic point of view, the morphology, particle size, and particle size distribution of catalysts are also key issues affecting the efficiency of reactions. Nano-photocatalysts have a high specific surface area, offering more gas/surface interaction, thereby enhancing the photocatalytic property[18]. In addition,

when the grain size becomes smaller, the diffusion length of deep charge carriers would be shortened to move on the photocatalyst surface, thus promoting the photocatalytic efficiency[17].

In this study, WO_3 nanoparticles were synthesized by co-precipitation method and doped with Fe^{3+} ions to improve the morphological, structural, and optical properties. The visible-light photocatalytic potential of pure and Fe-doped WO_3 samples was examined for the direct conversion of CO_2 in the gas phase. CH_4 was the reducing agent. GC and FTIR were applied for the study of photocatalytic activity and reaction products, respectively. A discussion on mechanism of photocatalytic reduction of CO_2 over Fe-doped WO_3 was also done. To the best of our knowledge, the photocatalytic reduction of CO_2 by WO_3 has been reported in only a few reports[19-24], and this paper is the first report on the visible-light photocatalytic reduction of CO_2 by Fe-doped WO_3 using CH_4 as reducing agent.

Experimental Section

Material

The used CO_2 and CH_4 gases were ultra-high pure (99.9%). $Na_2WO_4.2H_2O$ (99%), ethanol (96%), nitric acid (65%), hydrochloric acid (37%), and $FeCl_3.6H_2O$ were purchased from Merck (analytical grade). Deionized water, prepared from our lab, was also used in catalyst preparation. Stainless steel webnet with mesh sizes of 120 was used as support.

Photocatalyst synthesis

By a typical co-precipitation procedure, Fe-doped WO_3 nanoparticles, with different Fe doping concentrations of 0.00, 1.70, 4.18 atomic percentage (at.%), were synthesized as follows: 100 mL of $Na_2WO_4.2H_2O$ solution (0.5 M) was prepared and a required amount of $FeCl_3.6H_2O$ was added to the solution. The final solution was stirred magnetically for 30 min and heated at 80°C in a reflux. Hydrochloric acid (3.0 M) was added dropwise to the solution until precipitation. The resulting products were centrifuged and washed several times by deionized water to reach the natural *p*H of solution. During this period, nanoparticles were settled in the bottom of the centrifuge tube. Finally, the synthesized catalyst was dried at 50°C and calcined at 500°C for 2 h in air.

Photocatalyst immobilization on stainless steel webnet

To coat the stainless steel webnet with photocatalyst nanoparticles, a slurry containing the photocatalysts were prepared. To this aim, 1 g (± 0.01 g) of photocatalyst was poured to 20 mL ethanol to obtain the slurry. Then, 5 mL dilute nitric acid (*p*H 3.5 ± 0.01) was added to it to reach an uniform and semi-transparent slurry. The prepared slurry was sonicated for 30 min for suitable dispersion of powder and obtaining homogeneous slurry. By soaking the cleaned webnets in the slurry for 1 min, the photocatalyst particles were adsorbed on the support surface. The coated supports were put in an oven at 120°C (± 1.0°C) for 12 h for drying. In the final stage, they were annealed at 450°C (± 1.0°C) for 30 min. In all supported catalysts, 0.4 g (± 0.01 g) photocatalyst was coated on the support with 415 cm^2 (± 0.1 cm^2) mesh surface.

Characterization of photocatalyst and gaseous products

The room temperature XRD analysis was carried out by employing a SIEMENS D5000 (Germany) X-Ray Diffractometer with copper Kα (λ = 1.54 Å) radiation using a tube voltage and current of 40 kv and 40 mA respectively. The sample was scanned from 10-80° in 2θ with step size of 0.02° 2θ. FESEM images were obtained with a TESCAN FESEM instrument model MIRA3TESCAN-XMU operated at 15 kV. The samples were coated with a thin layer of gold before scanning for producing electric conductivity. Elemental composition was analyzed using an energy dispersive spectrometer (EDS or EDX) attached to the FESEM. The Raman spectra were recorded using Teksan spectroscopy (model: Takram P50C0R10) with 532 nm laser excitation (Nd:YAG laser) from 200 to 1000 cm^{-1} Diffuse-reflectance UV-vis spectra of the photocatalysts were recorded in the range 300–800 nm at room temperature using a Jasco V-670 spectrophotometer (Japan). Photoluminescence (PL) spectra of the products were recorded by a fluorescence spectrometer (Lumina; Thermo Fisher Scientific) with a 150 W Xenon lamp at an excitation wavelength of 375 nm.

Fourier-transform infrared spectroscopy (FTIR) was recorded using MB 160 FTIR spectrometer (ABB Bomem Inc., Canada). A cylindrical quartz cell with 3.5 cm diameter and 10 cm length was applied to characterize the photocatalysis products/intermediates in gaseous phase. The cell was closed with two Pyrex disks having KBr tablets with 1.2 cm diameter in center. Two inlet and outlet valves were embedded in the cell to fill and empty the gaseous sample. After a certain time, the designed cell was joined to the

output of the photoreactor to fill by the gaseous products of photocatalysis process, and then it was located in the spectrophotometer for recording the IR spectrum.

Photocatalysis experiments

Photocatalysis experiments of CO_2 conversionwere performed in a self-designed stainless steel batch photoreactor with an effective volume of 1000 mL. Figure 1 presents real photographs of the actual photoreactor system and the coated un-doped and Fe-doped WO_3 particles over the webnet. The cap of the photoreactor was sealed using O-rings and checked if there was leakage. At first, the reactor was vacuumed, and then it was fed by a gas stream composed of CO_2, CH4, and He (feed composition: 45%CO_2:45% CH_4:10%He) to 60 psig of absolute total pressure and allowed to reach gas–solid adsorption equilibrium. Before starting the reaction, the initial concentrations of CO_2 and CH_4 were measured using an on-line GC (equipped with a TCD detector). Once the concentration of CO_2 and CH_4 stabilized, the reaction was started by turning the lamp on (125 W high-pressure mercury lamp, Osram GmbH, Germany). By applying a glass

Fig. 1 — The real photographs of (a) assemble photoreactor, (b) coated cylindrical stainless steel webnets with un-doped and Fe-doped WO3 nanoparticles (c) open photoreactor with its cap, lamp situation, and also supported catalyst situation in the photoreactor vessel.

bulb having a special coating, the UV light was filtered out. The temperature of photocatalytic experiments was kept in 60°C. The concentrations of CO_2 and CH_4 were measured at 1 h intervals over a period of 5 h light illumination using GC-TCD. The photocatalytic activity was calculated on the basis of CO_2 and CH_4 conversions. Each experiment was performed in triplicate to make sure the reliability of the photocatalytic efficiency data.

Results and Discussion

Photocatalyst characterization

Figure 2 shows the XRD patterns of pure and Fe-doped WO_3 samples. All diffraction peaks in three samples are assigned to the monoclinic phase of WO_3 (JCPDS no. 05-0364). The XRD patterns of Fe doped samples are coincident with the pure WO_3, suggesting that Fe well incorporated into WO_3 lattice and there were no secondary phases (Fe_2O_3, Fe_3O_4, and Fe) because of very low concentration of Fe ions. In the monoclinic structure of WO_3, W^{6+} is octahedrally coordinated with O^{2-}. In iron oxides, the octahedral orientation has the higher crystal field stabilization energy of Fe^{3+} relative to the tetrahedral orientation[25]. Therefore, Fe^{3+} can fulfill the same coordination as W^{6+}, which means that Fe-doped WO_3 shows the same crystal structure as pure WO_3[26]. The observed shift in the peak position of Fe-doped WO_3 pattern, although very little (~ 0.1 Å), can be attributed to the small difference between ionic radii of Fe^{3+} and W^{6+}. The ionic radius of Fe^{3+} is slightly greater than that of W^{6+}, so a slight distortion in the crystal structure of Fe-doped WO_3 may happen, resulting in a shift in the diffraction peaks[25,26]. The average crystallite size, estimated by Scherrer's equation, was found to be ~14 nm for pure WO_3 and ~17 nm for two Fe-doped
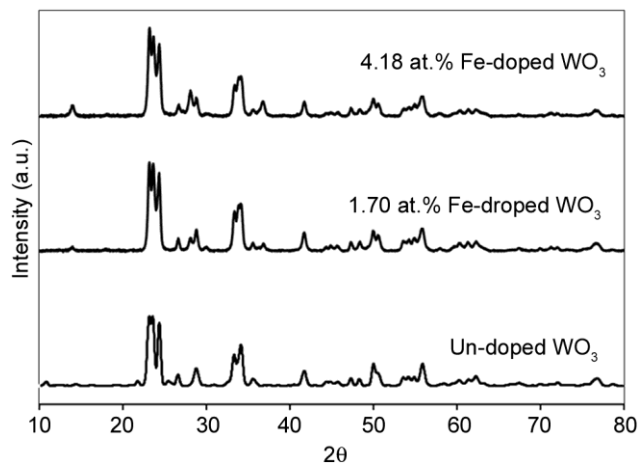

Fig. 2 — XRD patterns of the un-doped and Fe-doped WO3 nanoparticles.

samples, showing that the samples possess the nano-morphological aspect.

The FESEM images of pure and Fe-doped WO$_3$ nanoparticles coated on the support at different magnitudes are given in Fig. 3. The nanoparticles have an irregular shaped morphology, and the particles size of the Fe-doped samples seems to be slightly larger than that of the pure WO$_3$ sample. Also, the surface of Fe-doped WO$_3$/support thin film is rough and the grains appear to be densely packed compared to the pure WO$_3$ thin film.

The elemental mapping was applied to confirm the uniform distribution of Fe in the structure of the host matrix. The typical FESEM mapping pictures,

FESEM images and the corresponding EDX pattern of 0 and 4.18 at.% Fe-doped WO$_3$ are given in Fig. 4, respectively. The mapping and EDX results showed core levels of only W and O for pure WO$_3$ and W, O, and Fe for the Fe-doped WO$_3$ samples (Fig. 4b), indicating the high quality and purity of the photocatalysts. In addition, all the constituent elements of the doped samples, O (Fig. 4c), Fe (Fig. 4d), and W (Fig. 4e), were distributed uniformly.

Raman spectroscopy is commonly used to identify the molecules making up an unknown substance. Figure 5 shows Raman spectra of pure and Fe-doped WO$_3$ samples. One can see the major Raman peaks at 260, 323, 710, and 803 cm^{-1}, corresponding to the
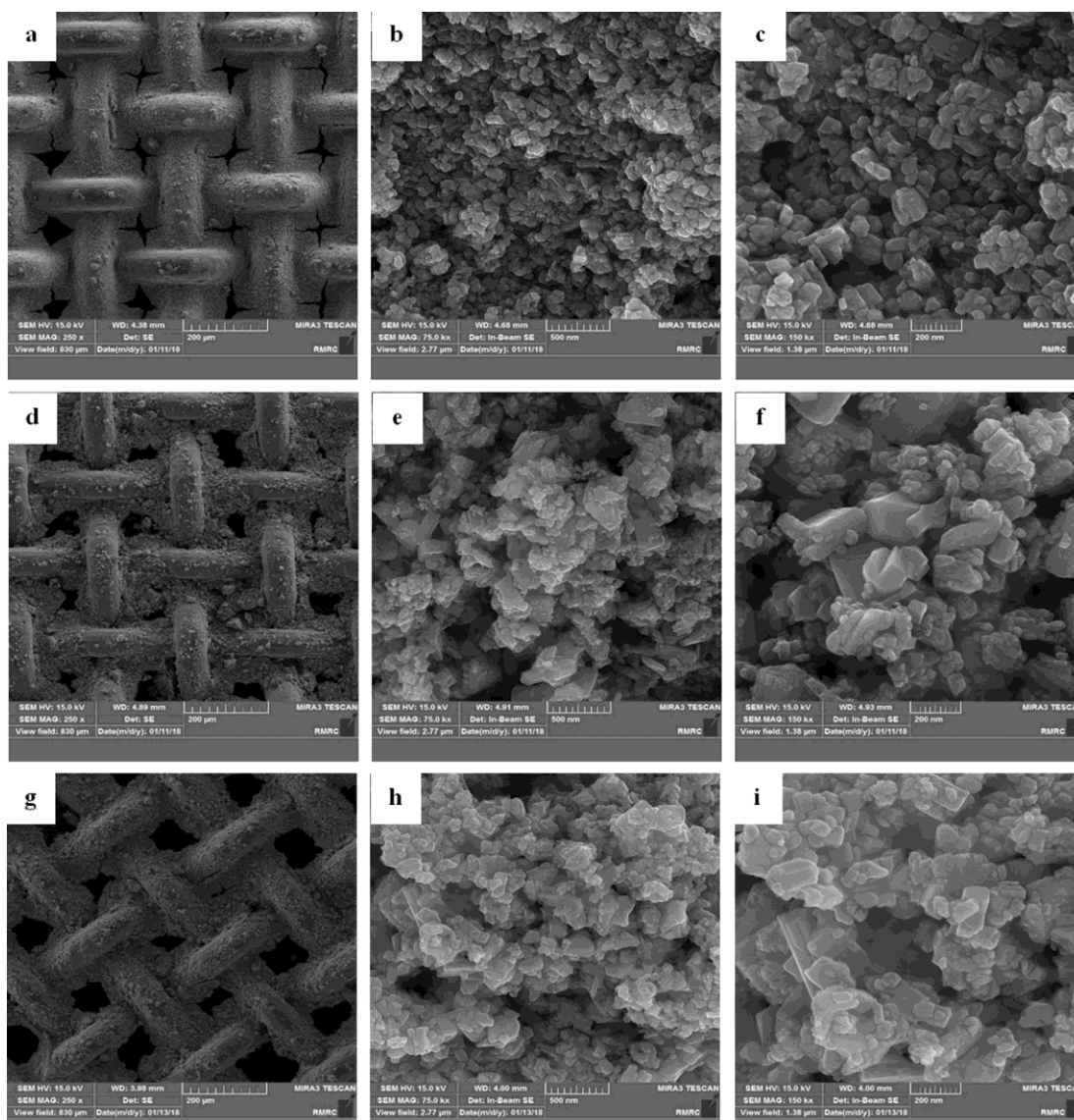

Fig. 3 — FESEM images of (a-c) un-doped WO3 nanoparticles/webnet, (d-f) 1.70 at.% Fe-doped WO3 nanoparticles/webnet, and (g-i) 4.18 at.% Fe-doped WO3 nanoparticles/webnet at different magnifications.

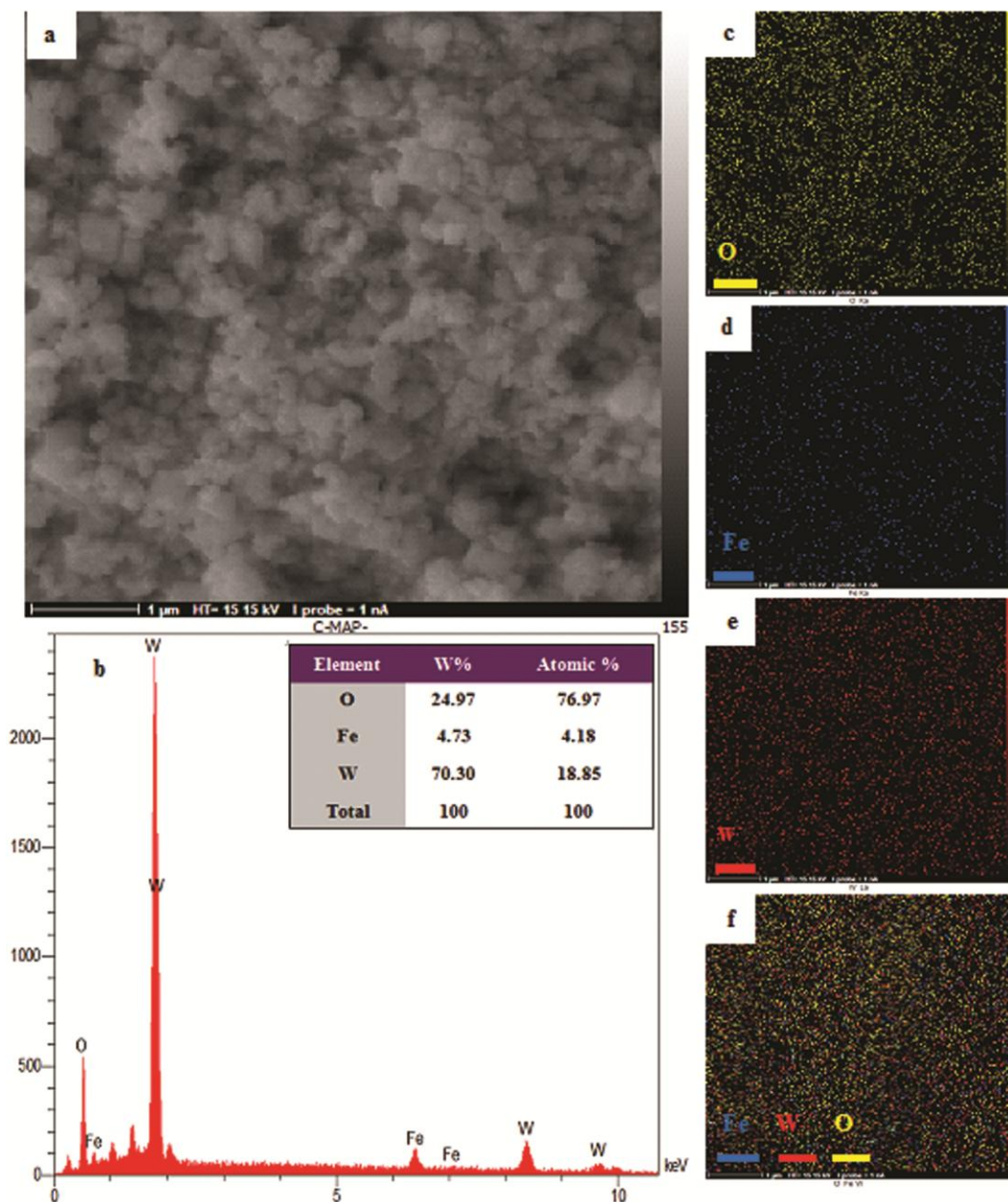| Element	W%	Atomic %
O	24.97	76.97
Fe	4.73	4.18
W	70.30	18.85
Total	100	100

Fig. 4 — Elemental mapping images of 4.18 at.% Fe-doped WO3 nanoparticles. (a) FESEM image, (b) EDX spectrum with data in the inset, and mapping data for (c) O, (d) Fe, (e) W, and (f) all three elements together.

Raman active modes of monoclinic WO_3 phase. The bands observed at 710 and 803 cm^{-1} are due to W−O stretching modes, and the others appeared at 260 and 323 cm^{-1} are attributed to the bridging oxygen modes[16]. A red shift in Raman spectra of Fe-doped WO_3 samples has been observed, arising from the replacement of the substitutional sites in WO_3 lattice by Fe ions. In addition, the structural defection made in WO_3 either by oxygen vacancy or by W^{6+} vacancy, as an inevitable consequence of doping treatment, is another reason for red shifting of Raman spectrum[16,27]. For all samples, the characteristic sodium tungstate bands at 940-960 cm^{-1} were not detected. Upon Fe doping, no other peak corresponding to the modes of Fe−O bonds is detected, which means the absence of any iron oxide. This observation is in agreement with the results of XRD.

The optical properties of the samples were studied by UV-vis technique (Fig. 6). A significant red shift is observed in the absorption wavelength onset by adding Fe ions into WO_3 lattice, indicating that Fe doping of WO_3 caused limitation of band gap. The band gaps of

the samples calculated by Kubelka-Munk functions[28]. As can be seen, with the increasing of Fe contents, the band gap of the samples decreased gradually. By Fe doping, a new donor level above the original valence band of WO_3 is created, and thus the overall band gap energy is limited[17]. It is apparent that the sample containing 4.18 at.% Fe can completely absorb visible-light photons having wavelength equal to/greater than ~ 500 nm, which is ideal for visible-light harvesting purposes. Given that the most intensity of solar radiation received to the Earth's surface is at green region (~560-520 nm), 4.18 at.% Fe-doped samples can be applied under solar radiation.

To investigate the effect of doping with Fe on recombination rate of charge carriers generated in WO_3, PL analysis was taken from all samples. As shown in Fig. 7, two main peaks at 421 and 488 nm are observed. The former belongs to photoluminescence emission by recombination of free excitons and is designated as near band edge emission (NBE), and the latter is blue emission caused by the structural defects that may act as donor or acceptor levels[29,30]. The intensity of these peaks decreased significantly by increasing Fe content. Thus, the most efficient charge carrier separation can be achieved by 4.18 at.% Fe-doped WO_3 sample. The PL signals illustrate that the dopant and defects play an important role in suppressing the electron-hole recombination, thereby increasing photocatalytic activity.
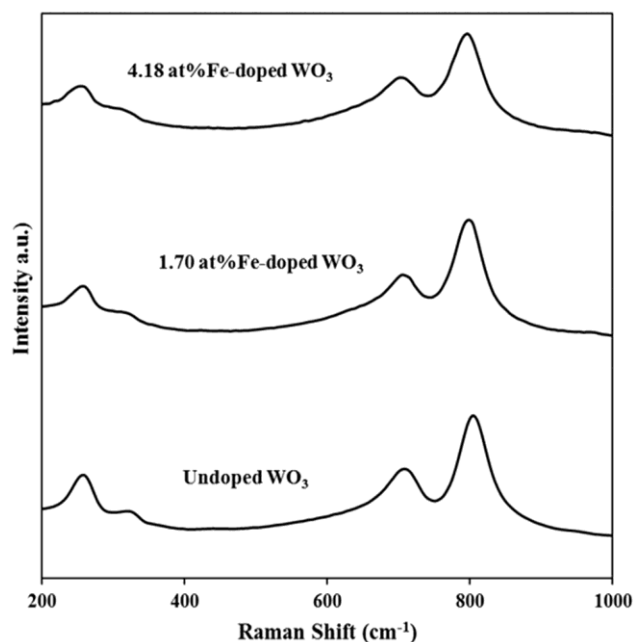
Photocatalytic activity

Figures 8 and 9 show the results of photocatalytic conversion of CO_2 and CH_4 by pure and Fe-doped WO_3 samples under visible-light irradiation, respectively. A series of blank experiments were taken to determine the effect of adsorption and photolysis on decreasing concentration of CO_2 and CH_4. It was established that no degradation occurred in these experiments, without illumination or photocatalyst. So, the photocatalytic conversion occurred only in the presence of both the light source and photocatalysts.

As can be seen, there is a significant photocatalytic redox potential in the conversion of CO_2 and CH_4 by WO_3 modified by iron under visible-light irradiation. The best visible-light photocatalytic activity was
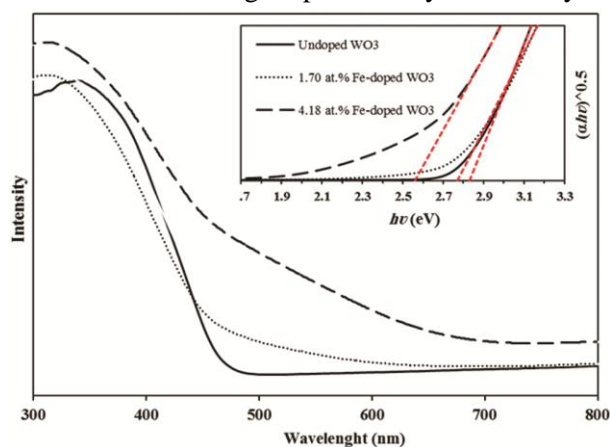

Fig. 6 — UV-Vis diffuse absorption spectra of the un-doped and Fe-doped WO3 nanoparticles (Inset shows the band energy gaps of the corresponding materials).
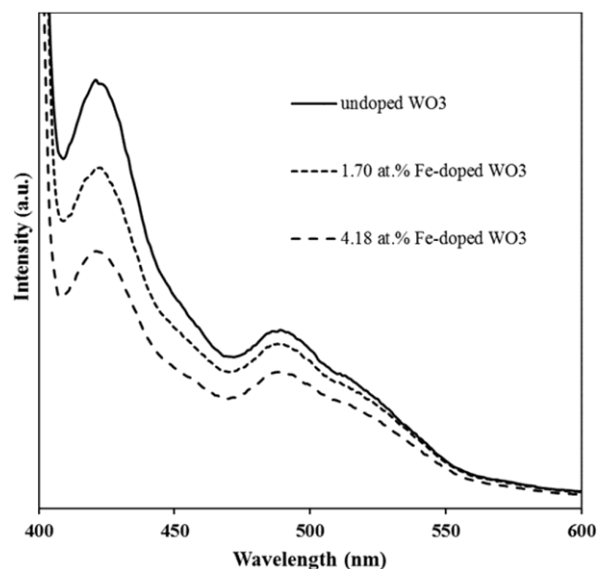

Fig. 5 — Raman spectra of the un-doped and Fe-doped WO3 nanoparticles.

Fig. 7 — Photoluminescence spectra of the un-doped and Fe-doped WO3 nanoparticles.
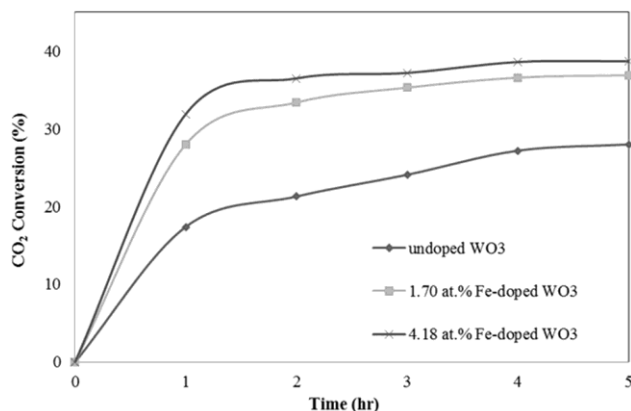
Fig. 8 — Photocatalytic reduction of CO2 under visible light illumination by un-doped and Fe-doped WO3 /webnetphotocatalysts.
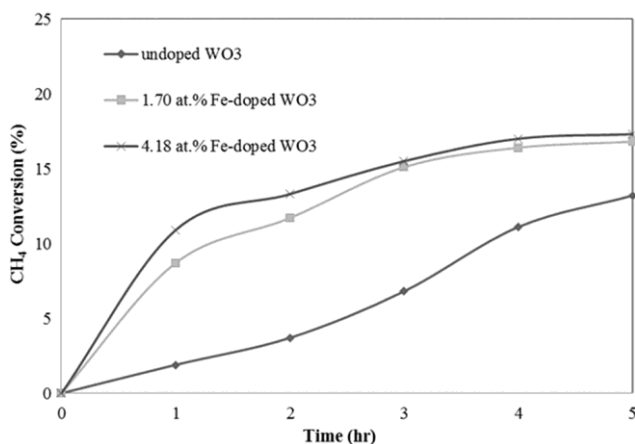

Fig. 9 — Photocatalytic oxidation of CH4 under visible light illumination by un-doped and Fe-doped WO_3 /webnetphotocatalysts.

found to be 38.7 and 17.3% for CO_2 and CH_4 by 4.18 at.% Fe-doped WO_3 sample, respectively. It must be noted that CH_4 not only is a reducing agent but also is a product of CO_2 photoreduction, so the actual amount of CH_4 conversion is greater than what we observed. There are two reasons to explain the improved photocatalytic activity. (I) As revealed by UV-vis analysis, doping with Fe significantly promoted the light absorption ability of WO_3 in the visible region, because of band gap limitation. Addition of Fe into WO_3 lattice creates a new dopant-energy level within the VB and CB of the pure sample. Thus, the visible light and longer-wavelength photons can effectively excite the electron-hole pairs. Based on UV-vis results, 4.18 at.% Fe-doped WO_3 sample has the best optical characteristic in the absorption of visible-light photons. (II) Another key parameter affecting the photocatalytic activity is the life time of electron-holes which was investigated by PL analysis. As shown by PL, the electron-hole recombination

strongly depends on the structural properties of WO_3 so that it is inhibited by increasing concentration of Fe in WO_3 up to 4.18 at.%. The sites of Fe ions and defects in the structure of WO_3 play act as trapping centers for photo-generated electron-holes and suppress the recombination rate.

From Figs. 8 and 9, the photocatalytic reactions seem to be saturated after 4 h experiment. Two reasons could explain why the photocatalysts were deactivated gradually with time: (I) The product accumulation on catalysts surface causes loss in accessible surface active sites for the target compounds. (II) The backward reactions leading to re-oxidizing photocatalytic products back into CO_2. This phenomenon occurs in the presence of O_2, and O_2 is an inevitable product of CO_2 conversion. Thus, it is reasonable that the photocatalytic conversion of CO_2 is saturated after a while. Liu et al.[31] claimed the desorption rate of acetate and formate from TiO2/WO3 surface was considerably lower than their catalytic oxidation rate, so these intermediates could significantly account for the decline in reaction rates by accumulating on the photocatalyst surface.

For practical applications, recycling heterogeneous catalysts is an important issue. We tried to regenerate the efficient photocatalyst (4.18 at.% Fe-doped WO_3) two times by heat treatment of the deactivated photocatalyst to desorb the surface species. The photocatalytic activity for CO_2 reduction was declined from 38.7 to 36.2 and 31.8% after each run. This result shows that the deactivated Fe-doped WO_3 samples can be effectively reused by a facile thermal treatment.
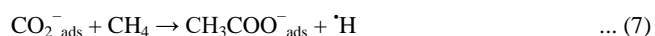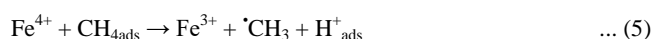
Discussion on the reaction mechanism

The photocatalytic conversion of CO_2 is a chain redox reaction generating light hydrocarbons and organic compounds like alkanes, alkenes, alcohols, ketones, aldehydes, and etc. CO has also been detected as either the primary product or the intermediate responsible for the production of the other organic chemicals[32]. In this research, ethane, formate and acetate derivatives were characterized to be the main products/intermediates detected by FTIR in the gas phase. The possible reaction pathways representing the formation of these products are proposed as follows.

At the first step of the charge transfer process, the surface active sites are generated by absorption of incident visible-light photons as given in Eqs. (1)-(3). Eqs. (2)-(3) clearly show the role of Fe sites in the

increase of life time of electron-holes where they involved in the inter-site charge transfer process. In fact, electron–hole pairs could be efficiently separated via doping the pure structure of WO_3 with Fe ions. On the CB side, CO_2 is first adsorbed on the catalyst surface and then reduced to anionic radical of $^\bullet CO_2^-$ by receiving electron (Eq. (4)). At the same time on the VB side, CH_4 is adsorbed on the catalyst surface and then oxidized to form $^\bullet CH_3$ upon a de-protonation process (Eq. (5)). The methyl radicals may undergo coupling to form ethane as shown in Eq. (6). Although, an alternative route for the ethane production is through five-steps $^\bullet CO_2^- \rightarrow CO \rightarrow ^\bullet CO^- \rightarrow ^\bullet C \rightarrow ^\bullet CH_3 \rightarrow C_2H_6$. When $^\bullet CO_2^-$ are attacked by CH_4 or by $^\bullet H$, acetone (Eqs. (7)-(8)) or formic acid (Eqs. (9)-(10)) could be formed, respectively. Given that both CO_2 and CH_4 are the carbon-based compounds, the formation of heavier products, like CH_3COOH, would be expected[33-36].

As discussed in reference[37], the localized oxygen vacancies are other active sites initiating photocatalytic reactions either by direct dissociation of CO_2 to CO ($CO_2 + [] \rightarrow CO + [O]$) or by reduction to CO via H on oxygen vacancy ($CO_2 + 2H^+ + 2e^- \rightarrow CO + H_2O$). CO then can be hydrogenated to the other products, C_2H_6, HCOOH, CH_3COOH.

$$WO_3 + h\nu \rightarrow e^- + h^+ \qquad \text{... (1)}$$

$$Fe^{3+} + e^- \rightarrow Fe^{2+} \qquad \text{... (2)}$$

$$Fe^{3+} + h^+ \rightarrow Fe^{4+} \qquad \text{... (3)}$$

$$Fe^{2+} + CO_{2ads} \rightarrow Fe^{3+} + {^\bullet CO_2^-}_{ads} \qquad \text{... (4)}$$

$$Fe^{4+} + CH_{4ads} \rightarrow Fe^{3+} + {^\bullet CH_3} + H^+_{ads} \qquad \text{... (5)}$$

$$CH_3 + {^\bullet CH_3} \rightarrow C_2H_6 \qquad \text{... (6)}$$

$${CO_2^-}_{ads} + CH_4 \rightarrow {CH_3COO^-}_{ads} + {^\bullet H} \qquad \text{... (7)}$$

$${CH_3COO^-}_{ads} + H^+ \rightarrow CH_3COOH \qquad \text{... (8)}$$

$${CO_2^-}_{ads} + {^\bullet H} \rightarrow {HCOO^-}_{ads} \qquad \text{... (9)}$$

$${HCOO^-}_{ads} + H^+ \rightarrow HCOOH \qquad \text{... (10)}$$
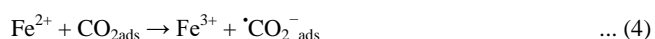
Conclusion

In summary, a series of Fe-doped WO_3 samples with different Fe concentrations are prepared, assessing visible-light photocatalytic conversion of CO_2 using CH_4 as the reducing agent. By a simple co-precipitation method, the nanoparticles are prepared with high crystalline quality and small grain size. Doping WO_3 with Fe resulted in efficient photocatalytic activity under visible-light due to two main reasons: (I) Narrowing band gap energy of WO_3 upon doping treatment, and (II) controlling recombination rate of charge carriers caused by the presence of Fe ions and structural defects. The best visible-light photocatalytic CO_2 reduction, 38.7%, is obtained by 4.18 at.% Fe-doped WO_3 sample. The major products of photocatalytic conversion of CO_2 and CH_4 are ethane, and formate and acetate derivatives. Because of the efficient photocatalytic activity in the green region of visible-light, 4.18 at.% Fe-doped WO_3 sample is recommended for the practical solar applications.

Abbreviations
CB: Conduction Band
EDX: Energy-Dispersive X-ray spectroscopy
FTIR: Fourier Transform Infrared Spectroscopy
FESEM: Field Emission Scanning Electron Microscopy
Fig. S: Figure in supplemental material file
GC: Gas Chromatography
GHGs: Greenhouse Gases
NBE: near band edge emission
PL: Photoluminescence spectroscopy
TCD: Thermal conductivity detector
UV-vis: Ultra Violet-Visible spectroscopy
VB: Valence Band
XRD: X-ray powder diffraction

References

1   Wu J C S, Lin H M & Lai C L, *Appl Catal A-Gen*, 296 (2005) 194.
2   Yadav S K & Mishra G C, *Inter J Eng Res Technol*, 6 (2013) 781.
3   Mahmodi G, Sharifnia S, Rahimpour F & Hosseini S N, *Sol Energ Mat & Sol C*, 111 (2013) 31.
4   Merajin M T, Sharifnia S, Hosseini S N & Yazdanpour N, *J Taiwan Inst Chem E*, 44 (2013) 239.
5   Tahir M & Amin N A S, *Energ Convers Manag*, 76 (2013) 194.
6   Dong P, Hou G, Xi X, Shao R & Dong F, *Environ Sci Nano*, 4 (2017) 539.
7   Sayama K, Hayashi H, Arai T, Yanagida M, Gunji T & Sugihara H, *Appl Catal B- Environ*, 94 (2010) 150.
8   Hameed A, Gondal M A & Yamani Z H, *Catal Commun*, 5 (2004) 715.
9   Hwang D W, Kim J, Park T J & Lee J S, *Catalysis Lett*, 80 (2002) 53.
10 Seddigi Z S, *B Environ Contam Tox*, 84 (2010) 564.
11 Kalanur S S & Seo H, *J Colloid Interf Sci*, 509 (2018) 440.
12 Karuppasamy K M & Subrahmanyam A, *J Phys D Appl Phys*, 41 (2008) 035302.
13 Deepa B & Rajendran V, Nano-Structures & Nano-Objects, 16 (2018) 185.
14 Wen Z, Wu W, Liu Z, Zhang H, Li J & Chen J, *Phys Chem Chem Phys*, 15 (2013) 6773.
15 Feng C, Wang S & Geng B, *Nanoscale*, 3 (2011) 3695.
16 Mehmood F, Iqbal J, Jan T & Mansoor Q, *J Alloy Compd*, 728 (2017) 1329.
17 Song H, Li Y, Lou Z, Xiao M, Hu L, Ye Z & Zhu L, *Appl Catal B-Environ*, 166 (2015) 112.
18 Moaddeli A & Abdollahi-Alibeik M, *J Porous Mat*, 25 (2018) 147.
19 Chen X, Zhou Y, Liu Q, Li Z, Liu J & Zou Z, *ACS Appl Mater Inter*, 4 (2012) 3372.

20 Jin J, Yu J, Guo D, Cui C & Ho W, *Small*, 11 (2015) 5262.
21 Ohno T, Murakami N, Koyanagi T & Yang Y, *J CO$_2$ Util*, 6 (2014) 17.
22 Wang P Q, Bai Y, Luo P Y, Liu J Y, *Catal Commun*, 38 (2013) 82.
23 Wang L, Wang Y, Cheng Y, Liu Z, Guo Q, Ha M N & Zhao Z, *J Mater Chem A*, 4 (2016) 5314.
24 Merajin M T, Nasiri M, Abedini E & Sharifnia S, *Indian J Chem Technol*, 25 (2018) 208.
25 Ahsan M, Tesfamichael T, Ionescu M, Bell J & Motta N, *Sensor Actuat B Chem*, 162 (2012) 14.
26 Zhang Z, haq M, Wen Z, Ye Z & Zhu L, *Appl Surf Sci*, 434 (2018) 891.
27 Upadhyay S B & Sahay P P, *Nano: Brief Reports Reviews*, 10 (2015) 1550113.
28 Ma G, Chen Z, Chen Z, Jin M, Meng Q, Yuan M, Wang X, Liu X & Zhou G, *Mater Today Energy*, 3 (2017) 45.

29 Ramkumar S & Rajarajan G, *J Mater Sci-Mater El*, 27 (2016) 1847.
30 Mukherjee R, Prajapati C S & Sahay P P, *J Therm Spray Technol*, 23 (2014) 1445.
31 Liu Y, Xie C, Zou T, Li J, Chen H & Zeng D, *Catal Commun*, 16 (2011) 180.
32 Corma A & Garcia H, *J Catal*, 308 (2013) 168.
33 Karamian E & Sharifnia S, *J CO$_2$ Util*, 16 (2016) 194.
34 Mahmodi G, Sharifnia S, Madani M & Vatanpour V, Sol Energy, 97 (2013) 186.
35 Merajin M T, Sharifnia S & Mansouri A M, *J Taiwan Inst Chem Eng*, 45 (2014) 869.
36 Yazdanpour N & Sharifnia S, *Sol Energy Mater Sol Cells*, 118 (2013) 1.
37 Ji Y & Luo Y, *J Am Chem Soc*, 138 (2016) 15896.